Quantitative tests revealing hydrogen-enhanced dislocation motion in α-iron

Longchao Huang [1,7], Dengke Chen [2,7], Degang Xie [1]✉, Suzhi Li [1], Yin Zhang[3], Ting Zhu [4], Dierk Raabe [5], En Ma[6], Ju Li [3] & Zhiwei Shan [1]✉

Hydrogen embrittlement jeopardizes the use of high-strength steels in critical load-bearing applications. However, uncertainty regarding how hydrogen affects dislocation motion, owing to the lack of quantitative experimental evidence, hinders our understanding of hydrogen embrittlement. Here, by studying the well-controlled, cyclic, bow-out motions of individual screw dislocations in α-iron, we find that the critical stress for initiating dislocation motion in a 2 Pa electron-beam-excited H_2 atmosphere is 27–43% lower than that in a vacuum environment, proving that hydrogen enhances screw dislocation motion. Moreover, we find that aside from vacuum degassing, cyclic loading and unloading facilitates the de-trapping of hydrogen, allowing the dislocation to regain its hydrogen-free behaviour. These findings at the individual dislocation level can inform hydrogen embrittlement modelling and guide the design of hydrogen-resistant steels.

In a hydrogen-based economy, the use of steels, which consist mainly of iron and often serve vital roles in power plants, vehicles, buildings or critical infrastructures, is at risk owing to hydrogen embrittlement—a sudden and often catastrophic deterioration of the material's load-bearing capacity. Although multiple hydrogen embrittlement mechanisms[1–5] have been proposed, a consensus has yet to be reached on the effects of these embrittlement modes. Also, direct experimental proof of the influence of hydrogen at the single dislocation level is missing. Challenges arise from the formidable complexity of the hydrogen embrittlement phenomenon, owing to the often intricate interplay of several mechanisms. Consequently, some reported macroscopic observations are contradictory. At the macroscale, hydrogen has been shown to cause both hardening and softening in pure iron[6,7], while in regions below the fracture surface, hydrogen has been found to either enhance[8,9] or reduce[10,11] plastic activity. At the micro- and nanoscales, the main debate revolves around the effect of hydrogen on the energetics and kinetics of dislocations[12–17]. According to the classic Cottrell and Snoek theories, diffusible interstitial atoms including hydrogen are expected to form an atmosphere around the dislocation, causing a drag force acting against dislocation motion[18,19]. Interestingly, Birnbaum, Robertson and coworkers observed the opposite, namely, the mobility of dislocations was increased in several metallic materials when exposed to hydrogen[20–24]. They attributed this to elastic shielding of the dislocation's stress field by the hydrogen atmosphere that was assumed to surround the dislocation core. The hydrogen-enhanced dislocation mobility was proposed as the 'root cause' of hydrogen embrittlement, serving as core evidence for the hydrogen-enhanced localized plasticity (HELP) mechanism[2]. However, these results have been challenged by recent atomistic simulations, which did not reproduce hydrogen-enhanced dislocation mobility but instead showed a hydrogen-induced drag effect in aluminium[25] and α-iron[26]. On the experimental side, we confirmed some of these theoretical hypotheses,

[1]Center for Advancing Materials Performance from the Nanoscale (CAMP-Nano), State Key Laboratory for Mechanical Behavior of Materials, Xi'an Jiaotong University, Xi'an, People's Republic of China. [2]Department of Engineering Mechanics, School of Naval Architecture, Ocean and Civil Engineering, Shanghai Jiao Tong University, Shanghai, People's Republic of China. [3]Department of Nuclear Science and Engineering and Department of Materials Science and Engineering, Massachusetts Institute of Technology, Cambridge, MA, USA. [4]Woodruff School of Mechanical Engineering, Georgia Institute of Technology, Atlanta, GA, USA. [5]Max-Planck-Institut für Eisenforschung, Düsseldorf, Germany. [6]Center for Alloy Innovation and Design (CAID), State Key Laboratory for Mechanical Behavior of Materials, Xi'an Jiaotong University, Xi'an, People's Republic of China. [7]These authors contributed equally: Longchao Huang, Dengke Chen. ✉e-mail: dg_xie@xjtu.edu.cn; zwshan@xjtu.edu.cn

namely, a hydrogen-induced pinning effect of dislocations[25], for the case of aluminium, which has a face-centred-cubic structure and contains narrow stacking faults. For metals with a body-centred-cubic (bcc) structure, such as α-iron, tungsten and so on, the motion of screw dislocation via kink-pair formation and propagation is the rate-controlling process of deformation at room temperature[27,28]. However, direct experimental observations that clearly reveal the hydrogen effect on screw dislocation motion at the single-defect scale are still lacking despite earlier models and atomistic simulations[15,16,29,30].

In the classic works by Birnbaum, Robertson and co-workers, their experimental set-up was designed to change the hydrogen atmosphere during or after dislocation glide in an environmental transmission electron microscope (ETEM)[20–24]. However, there are a few unclear issues about the experimental set-up they used for revealing the hydrogen effect on dislocation mobility. First, before hydrogen introduction, the observed dislocations were usually at rest[21–23], thus making it impossible to observe any hydrogen-related drag or pinning effects. Second, when thousands of pascals of H_2 gas were flooded into or pumped out of the ETEM chamber within a few seconds, this might have altered either the local distribution of internal stresses or the external load, which had been assumed to remain constant. These effects might have triggered dislocation motion due to their high sensitivity to stress. Finally, as the dislocations move by dragging pinning points on the foil surfaces[20,23,24], the velocity of a dislocation would be largely determined by the pinning effect at both dislocation ends. However, dislocation pinning can be altered by possible hydrogen-induced reduction of the surface oxides or removal of organic contaminants from the surface under electron beam illumination[31]. These considerations fuel our motivation to perform well-controlled experiments that are capable of reducing the impact of these factors substantially, particularly related to uncontrolled surface pinning of dislocations.

In this Article, we designed a fully quantitative in situ ETEM mechanical testing protocol, as illustrated in Fig. 1, that enables the observation and comparison of bow-out motion of the same dislocation segments under a vacuum and in a hydrogen-containing environment. To avoid the thin-foil problems described above, we prepared submicrometre-sized free-standing cylindrical α-iron pillars, which were subjected to cyclic stresses with the aim to remove most of the pre-existing dislocations (referred to as the mechanical annealing effect[32]) while retaining a few individually isolated screw dislocations that showed well-controlled bow-out motion between the pinning points (Fig. 1b,c; also Supplementary Fig. 1 and Supplementary Note 1). In the bow-out motion, the dislocation moves with increasing applied stress by gradually changing from a straight to a bowed-out configuration, as shown in Fig. 1c. Upon unloading, the dislocation segment springs back to its original equilibrium shape and position, indicating that the bow-out motion is reversible and no new pinning in the temporarily sheared region had taken place. This controlled dislocation motion was exactly repeated in a series of testing cycles by maintaining a constant low magnitude of cyclic stress (locally depending on bow-out stress), thus allowing for quantifying the variation in dislocation responses, for example, the stress required for activating the movement of each individual dislocation and its glide distance, upon varied environmental conditions in a highly controlled manner, as shown in Fig. 1d. Compared with previous experiments, our experimental set-up reduces the influence of the possible variation of surface and boundary conditions and inhomogeneous stresses on dislocation motion.

Figure 2a shows a typical dislocation (marked as 1) that showed stable and fully reversible bow-out motion under cyclic compression. It is a predominant screw type with the Burgers vector ½<111> on the {112} slip plane (Supplementary Figs. 2 and 3 and Supplementary Table 1). The testing started with a session under vacuum (before hydrogenation), which consisted of a total of 11 consecutive load cycles numbered $N = 1–11$ (Supplementary Video 1). Identical load-time functions were
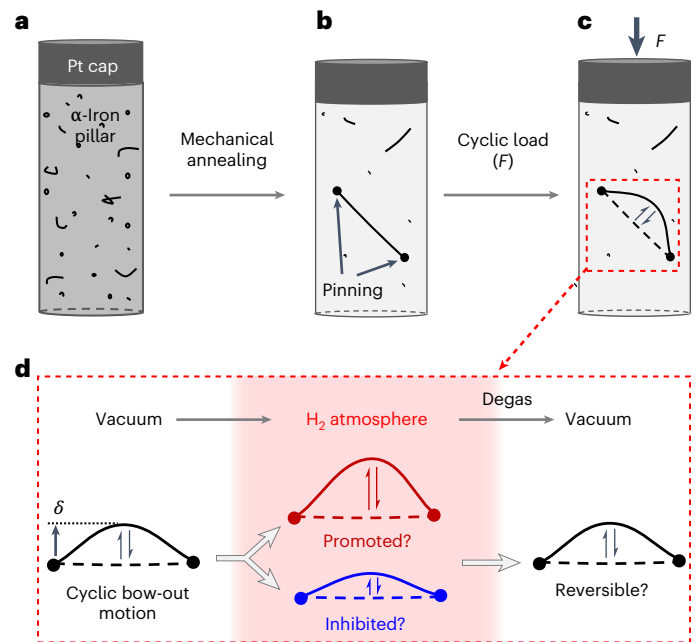
Fig. 1 | Schematic of the experimental set-up for revealing the effect of hydrogen on dislocation motion. a, The as-fabricated single-crystal iron pillar with a platinum cap at the top, to provide well-controlled contact conditions. **b**, The pillar after mechanical annealing treatment (see the text), which eliminates most pre-existing dislocations while retaining several long screw-type dislocations with both ends pinned. **c**, Under cyclic compression loads (F) with engineering stress ranging from the minimum (σ_{min}) to the maximum (σ_{max}), dislocation segments between pinning points accordingly move forward and back. The dashed line shows their shape and position at σ_{min}. **d**, The sequential cyclic compression experiments under varying testing atmosphere (vacuum, hydrogen) to compare the dislocation motion under well-defined mechanical and atmospheric boundary conditions.

applied to all cycles, resulting in a normal stress oscillation between the valley stress (σ_{min}) of ~21 MPa and the peak stress (σ_{max}) of ~211 MPa. The bow-out motion was stable, fully reversible and reproducible during the first test session in vacuum (Supplementary Fig. 4a,b). Subsequently, we exposed the sample to ~2 Pa H_2 under electron illumination for about 2 h. Previous experiments have shown that when the 2 Pa H_2 is excited by the high-voltage electron beam, the equivalent fugacity can reach hundreds of megapascals[33]. Using Sieverts' law[34] and 500 MPa hydrogen fugacity, the equilibrium lattice concentration of hydrogen in iron was estimated to be ~2 atomic ppm. Although the concentration of hydrogen at the dislocation core could be much higher, the dislocation configuration was observed to remain unchanged throughout the hydrogenation process (Supplementary Fig. 4b,c).

After hydrogenation, we applied the same load-time function for the ensuing load cycles (renumbered $N = 1, 2, ..., 12$) (Supplementary Video 2). Before we compared the movements of dislocation 1 without and with hydrogen exposure, we confirmed again that the bow-out motion was stable and fully reversible and the microstructure inside the pillar remained unchanged after a total of 12 loading cycles under 2 Pa H_2 atmosphere, as shown in Supplementary Fig. 4c,d, ensuring a reliable comparison. Then we observed that in 2 Pa H_2, the bow-out movement of dislocation 1 showed an increased amplitude, as indicated by comparison of its configuration at σ_{max} in vacuum and in the hydrogenated state (Fig. 2b). To further quantify the hydrogenation-induced change in dislocation motion, we performed a frame-by-frame correlation between loading time or stress and the position of dislocation 1 in the video recorded during the whole in situ test. In each cycle, the movement of dislocation 1 became activated only when the applied stress was increased above a critical value referred to as the dislocation activation
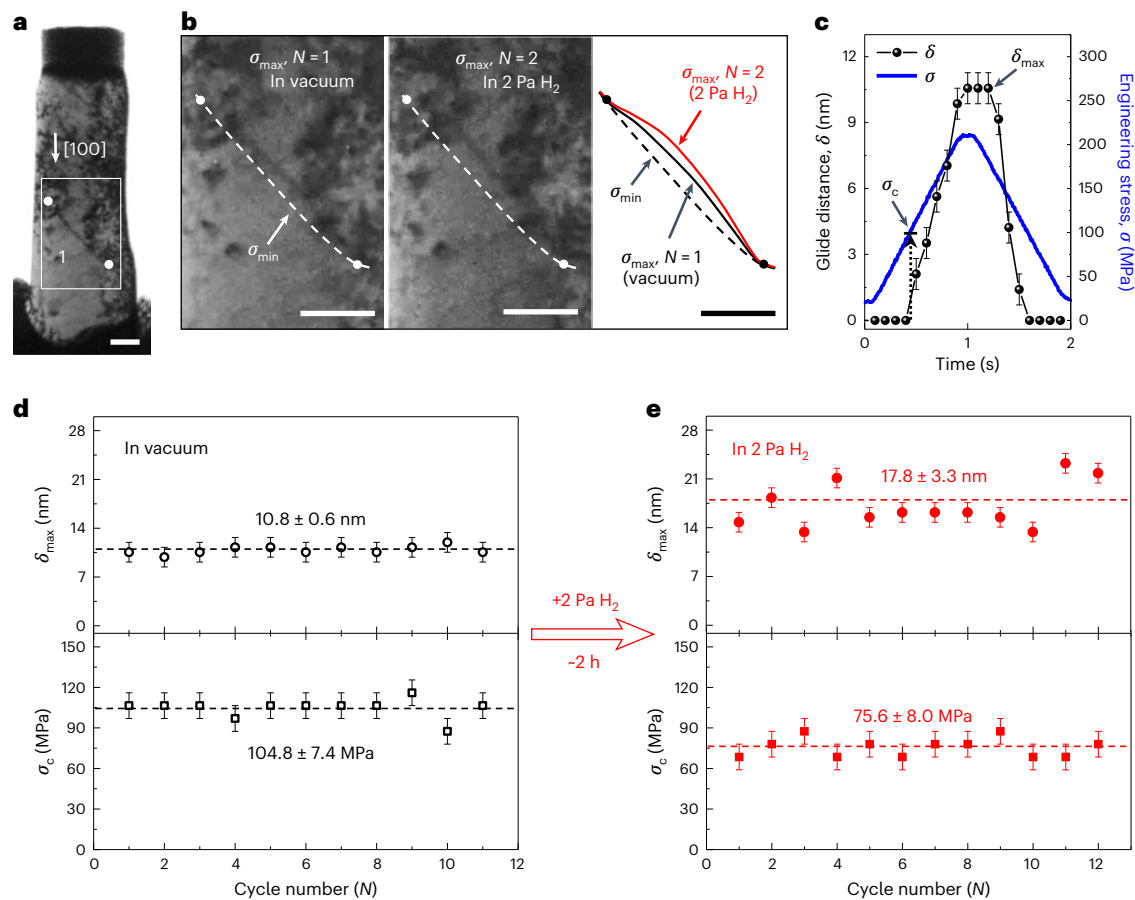
Fig. 2 | Effect of hydrogenation on the bow-out motion of a screw dislocation. **a**, Bright-field transmission electron microscope image showing the pillar after a series of cyclic compression loading and unloading sessions (as detailed in Supplementary Fig. 1). A mobile dislocation tagged as 1 in the boxed region is magnified and observed in **b**. The white spots indicate the pinning points. **b**, Configurations of dislocation 1 at σ_{max} in vacuum ($N = 1$) and in 2 Pa H_2 ($N = 2$). The shape and position of dislocation 1 at σ_{min}, which is the same as that under the unloaded state, as shown in **a**, is delineated with a white dashed line and used as a reference position and shape. The superimposed profiles of dislocation 1 in different states are illustrated on the rightmost. **c**, The loading engineering stress σ and the digitally tracked projected glide distance δ of dislocation 1 in a typical load cycle are shown as a function of time. The critical stress for activating the dislocation (σ_c) and the maximum glide distance (δ_{max}) are also indicated. **d,e**, The measured δ_{max} and σ_c of dislocation 1 as a function of loading cycle number in vacuum (**d**) and in 2 Pa H_2 (**e**). Errors for measurements of δ_{max} and σ_c are ±1.4 nm and ±9.5 MPa, respectively. Error bars represent standard deviation. The tests in 2 Pa H_2 were started after the pillar had been exposed to the 2 Pa H_2 atmosphere for ~2 h. Scale bars, 100 nm.

stress (σ_c). Then the dislocation continued to glide, until it reached the maximum projected bow-out displacement (δ_{max}) at the peak stress σ_{max}, as shown in Fig. 2c. The measured δ_{max} and σ_c in each cycle (Fig. 2d,e) confirmed that the bow-out of dislocation 1 after hydrogenation can reach a larger distance than that under vacuum, and the average δ_{max} increased by ~65% from 10.8 ± 0.6 nm in vacuum to 17.8 ± 3.3 nm under the hydrogen environment. Moreover, the average σ_c was reduced by ~28% from 104.8 ± 7.4 MPa to 75.6 ± 8.0 MPa after hydrogenation. These effects of hydrogen on the motion of the screw dislocation were further corroborated by another series of controlled testing (Supplementary Note 2, Supplementary Fig. 5, and Supplementary Videos 3 and 4), showing ~27% lower σ_c and ~64% larger δ_{max} for dislocation motion after hydrogenation. Effects from the near-surface defects that remained in the pillar can be reasonably excluded (Supplementary Note 3 and Supplementary Fig. 6). Therefore, our experimental results prove that the screw dislocation moves easier (with 27–28% lower stress and 64–65% larger bow-out distance under the same applied load) after exposure to 2 Pa H_2 excited by an electron beam. Evidently, hydrogen substantially enhances the screw dislocation motion in α-iron.

In addition, we noticed that for the reference experiments described above, if the dislocation completely moves out of the hydrogen atmosphere, it is expected to move with a δ_{max} value close

to that in vacuum during its ensuing motion. The observed increase of δ_{max} in almost all cycles after hydrogenation thus indicates that the hydrogen atmosphere moves together with the dislocation during its bow-out motion. Therefore, the enhanced dislocation mobility should originate from direct interaction between the dislocation and the hydrogen atoms whose diffusion matches the dislocation velocity.

It is worth noting that our experiments prove the phenomenon of hydrogen-enhanced screw dislocation motion only for the case of low hydrogen concentrations. With increasing hydrogen concentration, it is possible that the hydrogen-drag effect might become important[16]. Indeed, our previous experimental work has shown hydrogen-inhibited dislocation motion in face-centred-cubic aluminium[25], due to hydrogenated vacancies rather than interstitial hydrogen atoms. Such hydrogenated vacancies, of which the formation could be enhanced by hydrogen during plastic deformation[4], have also been reported to impose large resistance to motion of dislocations in bcc metals[5,35]. These experimental results and simulations indicate that the hydrogen-dislocation interaction varies with the material, dislocation type, hydrogen and vacancy concentrations. In our study, the drag effect caused by hydrogenated vacancies is not dominant in the α-iron pillars. This implies that superabundant vacancies had not
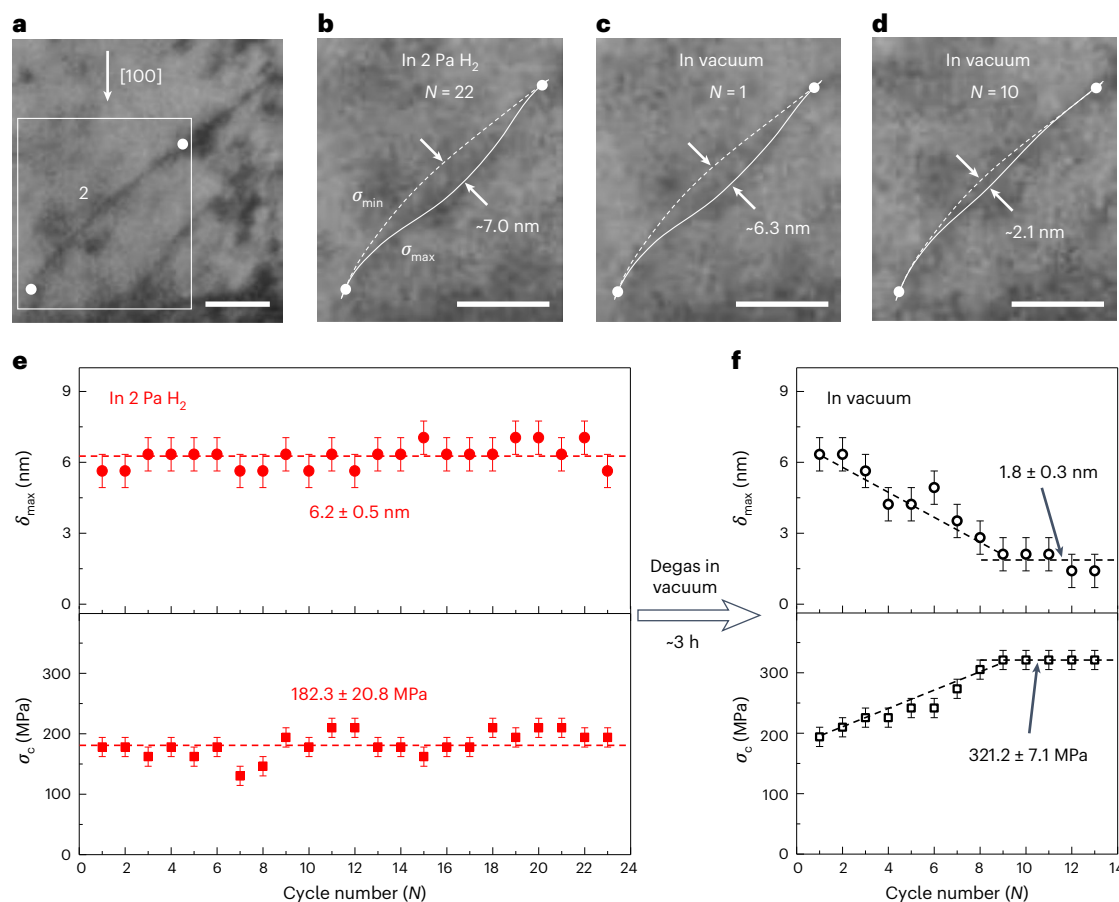
Fig. 3 | Effect of hydrogen degassing on dislocation behaviour. a, Mobile dislocation 2 at σ_{min} (~35 MPa). The mobile segment of dislocation 2 is located in the boxed area that is magnified and observed in **b**–**d**, in which its profile is delineated as a white dashed line and used as a reference position and shape. **b**–**d**, Dislocation motion of a few chosen cycles before ($N = 22$ (**b**)) and after ($N = 1$ (**c**) and 10 (**d**)) switching back to vacuum. The profiles of dislocation 2 at σ_{max} (~355 MPa) are delineated with white solid lines. **e,f**, The measured δ_{max} and σ_c of dislocation 2 in each cycle in 2 Pa H_2 (**e**) and in vacuum (**f**). Errors for measurements of δ_{max} and σ_c are ±0.7 nm and ±15.9 MPa, respectively. Error bars represent standard deviation. The tests in vacuum were started after the sample had been degassed in vacuum for ~3 h. Scale bars, 50 nm.

formed under our experimental conditions (for example, in the early stage of plastic deformation).

Next, we studied whether the dislocation response could be reversed after switching the hydrogen environment back to vacuum. In the loading cycles in 2 Pa H_2 that followed $N = 12$, the configuration of dislocation 1 changed due to an accidental depinning event. Hence, we had to increase the stress amplitude of the following loading session, to introduce another similar dislocation (marked as 2 in Fig. 3a). This dislocation showed stable bow-out motion (Supplementary Video 5) under cyclic loading between σ_{min} (~35 MPa) and σ_{max} (~353 MPa). The stress-induced change in shapes and positions of dislocation 2 in cycles before and after degassing are shown in Fig. 3b–d. Throughout all the 23 load cycles during the testing session immediately before degassing, the stress-driven dislocation motion was almost the same, with the average $\delta_{max} = 6.2 \pm 0.5$ nm and $\sigma_c = 182.3 \pm 20.8$ MPa. Then, the hydrogen inlet was closed. Within only 2 min, the specimen chamber of the ETEM was pumped to high vacuum (<5 × 10^{-4} Pa). In the following 3 h, the sample stayed under vacuum for further degassing. Such a long degassing time was sufficient for hydrogen in the sample to reach a new equilibrium distribution. After degassing, we applied the same cyclic load. In the first cycle, the dislocation moved to almost the same δ_{max} as that in the cycles before degassing. But in the ensuing 8 load cycles, the average δ_{max} of dislocation 2 gradually decreased, from 6.2 nm to 1.8 nm (Fig. 3b–f and Supplementary Video 6). Meanwhile, the measured σ_c after degassing remained at the first reload cycle and then gradually

increased until reaching a plateau value of 321.2 ± 7.1 MPa after the 9th cycle, showing an ~43% lower activation stress σ_c in the hydrogenated state than the hydrogen-free state (Fig. 3e,f). These results show the reversible nature of the hydrogen-dislocation interaction, consistent with the recovery of conventional plastic flow observed in bulk metals with low hydrogen concentrations after degassing[6].

We note that the recovery of the dislocation response after switching back to vacuum was unexpectedly slow, as even after ~3 h of degassing in vacuum, it still took ~20 s, or ~10 load cycles, for dislocation 2 to gradually recover its stable cyclic motion under vacuum. With the high diffusivity of hydrogen in α-iron (D_H, of the order of 10^{-9} to 10^{-8} m^2 s^{-1} at room temperature[36]), the time for hydrogen to diffuse out of the pillar was estimated to be less than 1 s according to $\lambda^2/4D_H$ (with $\lambda \approx 1,000$ nm being the characteristic length scale). This means that the time lapse (2 s) during each individual load cycle was sufficient for hydrogen to redistribute and reach a new equilibrium distribution inside the pillar. Given that the full restoration of dislocation behaviour after switching from hydrogen back to vacuum requires multiple load cycles, hydrogen traps should play a critical role in the overall recovery kinetics. Even after hours of ageing in vacuum, the traps could still retain a certain amount of hydrogen, which was released only slowly during the ensuing load cycles, so that its effect on dislocation motion remained active until the hydrogen stored in these traps was gradually decreased below a critical level. Considering that no strong hydrogen traps, such as grain boundaries or precipitates, were present in our
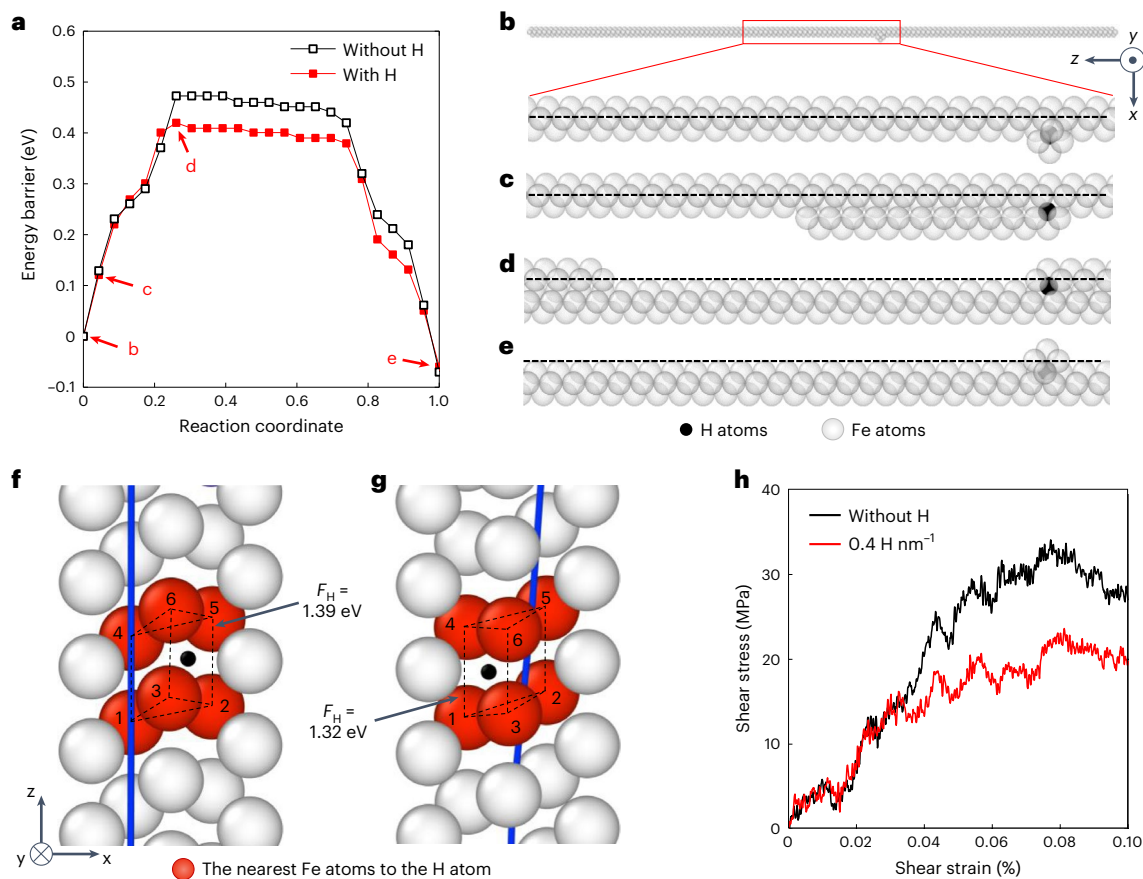
Fig. 4 | Atomistic mechanism of hydrogen-enhanced screw dislocation glide. a, Representative MEPs of screw dislocation glide without and with a hydrogen atom in the dislocation core under a resolved shear stress τ_{yz} = 24 MPa. **b–e**, Sequential atomic configurations of kink nucleation process along the screw dislocation line in the presence of a hydrogen atom, with the corresponding energy of each configuration indicated by a red arrow in **a**. Here the hydrogen atom is represented by a black sphere, while the iron atoms are represented by grey spheres. **f**, The magnified atomic configuration around the hydrogen atom at the initial state along the MEP with H in **a**. **g**, The same as in **f** except for the saddle-point state. The six iron atoms surrounding the interstitial H atom (small black sphere) are coloured in red and labelled by 1–6, forming a polyhedron. The current effective position of this screw dislocation is indicated by a blue line in **f** and **g**, respectively. **h**, Molecular dynamics simulation results of mean stress–strain curves without and with hydrogen atoms.

sample, the delayed restoration of the dislocation behaviour should originate from other traps, such as dislocations and vacancies[37,38]. The fact that the hydrogen-induced enhancement in dislocation motion gradually diminishes with successive oscillating motion of dislocations suggests that cyclic loading and unloading facilitates degassing of hydrogen from those weak hydrogen traps, allowing the dislocation to regain its hydrogen-free behaviour. A detailed discussion of this mechanically-assisted degassing effect is provided in Supplementary Note 4.

Our experimental results on hydrogen-enhanced dislocation motion reveal two major effects, that is, the decrease of activation stress and the increase of bow-out displacement. The former is obtained from direct measurement of a stress corresponding to the initiation of motion from a nearly straight screw dislocation, which is usually controlled by the nucleation and propagation of kink pairs. The latter is from direct ETEM observation and can be dictated by a competition between the hydrogen-affected dislocation line tension and kink-pair activity. To investigate the underlying mechanisms of hydrogen-induced reduction in activation stress, we performed atomistic simulations using the nudged elastic band (NEB) method[39,40]. A series of NEB calculations allow us to determine the minimum energy paths (MEPs) and associated activation energies of dislocation motion with and without hydrogen atoms at the dislocation core, respectively. The NEB results in Fig. 4a reveal the representative MEPs of screw dislocation glide under a resolved shear stress τ_{yz} = 24 MPa (Supplementary

Note 5). Similar to the previous NEB results in bcc metals without hydrogen[41,42], it is the correlated kink nucleation that controls the activation process of screw dislocation glide. In particular, the hydrogen atom provides a favourable site for kink nucleation (Fig. 4b,c), leading to a lower energy barrier (from energy barrier without hydrogen E = 0.47 eV to energy barrier with hydrogen E_H = 0.42 eV) for screw dislocation glide. In addition, as shown in Supplementary Fig. 7, the decrease of energy barrier ($\Delta E = E - E_H$ = 0.05 eV) is not sensitive to the range of resolved shear stresses applied (τ_{yz} = 0–58 MPa).

We further evaluated the binding energy difference of hydrogen at various positions along the core of a screw dislocation line via tracking the intermediate atomic configurations of the kink nucleation process around the hydrogen atom, as shown in Fig. 4f,g. The interaction energy between Fe and H is mainly governed by the embedding energy, which is a function of local electron density at the interstitial site[43], that is, a polyhedron consisting of six nearest iron atoms surrounding a hydrogen atom. Our atomistic calculations (Supplementary Note 6) show that the normalized electron density (ρ_H = 45.4) surrounding a hydrogen atom arising from six nearest iron atoms in the initial configuration is larger than that (ρ_H = 44.7) in the saddle-point configuration. Consequently, the embedding energy function F_H decreases approximately from 1.39 eV to 1.32 eV with decreasing ρ_H. This results in the reduction of kink-pair nucleation barrier. In other words, the hydrogen atoms promote kink nucleation and decrease the critical stress of dislocation glide. This effect is also supported by molecular dynamics simulations.

In Fig. 4h, we compare the molecular-dynamics-simulated stress–strain curves of screw dislocation glide with and without hydrogen at room temperature. With randomly distributed hydrogen atoms around the dislocation core (0.4 hydrogen atom per nanometre), the critical shear stress of dislocation glide decreases from 32 MPa to 22 MPa. This molecular dynamics result agrees qualitatively with our experimental measurements, namely, the activation shear stress (τ_c) of dislocation 1 reduces from 49.4 MPa to 35.6 MPa, as calculated with the Schmid factor of the most favoured {112}<111> slip system.

In non-hydride-forming metals, the HELP mechanism is often considered as a key factor contributing to hydrogen embrittlement, and it is supported by metallographic features stemming from enhanced dislocation activity beneath either intergranular or transgranular fracture surfaces in iron and steels[8,44]. One critical element of the HELP mechanism is the hydrogen-enhanced dislocation activity (for example, mobility) in the early and intermediate stages of plastic deformation, before the formation of microvoids. This is usually interpreted as a result of the elastic shielding effect by hydrogen, which has been proposed on the basis of experimental observations of the hydrogen-induced reduction in spacings among piled-up edge dislocations[45]. In this Article, we provide compelling experimental evidence of hydrogen-enhanced screw dislocation motion in α-iron. The hydrogen-induced decrease of dislocation activation stress in the experiment is consistent with the decrease of kink-pair nucleation barrier caused by hydrogen in atomistic simulation. These results indicate that the hydrogen effect on kink-pair nucleation could be the underlying mechanism of enhanced dislocation motion when the dislocation line is almost straight. However, the primary factor controlling the increased extent of dislocation bow-out by hydrogen remains uncertain. This is because hydrogen could not only lower the kink-pair nucleation barrier on a bow-out dislocation but also reduce the dislocation line tension to lower the dislocation bow-out stress, leading to an increased extent of dislocation bow-out. These uncertainties warrant further study in the future.

Online content

Any methods, additional references, Nature Portfolio reporting summaries, source data, extended data, supplementary information, acknowledgements, peer review information; details of author contributions and competing interests; and statements of data and code availability are available at https://doi.org/10.1038/s41563-023-01537-w.

References

1. Beachem, C. D. A new model for hydrogen-assisted cracking (hydrogen 'embrittlement'). *Metall. Mater. Trans. B* **3**, 441–455 (1972).
2. Birnbaum, H. K. & Sofronis, P. Hydrogen-enhanced localized plasticity—a mechanism for hydrogen-related fracture. *Mater. Sci. Eng. A* **176**, 191–202 (1994).
3. Oriani, R. A. A mechanistic theory of hydrogen embrittlement of steels. *Ber. Bunsenges. Phys. Chem.* **76**, 848–857 (1972).
4. Sakaki, K. et al. The effect of hydrogen on vacancy generation in iron by plastic deformation. *Scr. Mater.* **55**, 1031–1034 (2006).
5. Li, S. et al. The interaction of dislocations and hydrogen-vacancy complexes and its importance for deformation-induced proto nano-voids formation in α-Fe. *Int. J. Plast.* **74**, 175–191 (2015).
6. Kimura, A. & Birnbaum, H. K. Plastic softening by hydrogen plasma charging in pure iron. *Scr. Metall. Mater.* **21**, 53–57 (1987).
7. Matsui, H., Kimura, H. & Moriya, S. The effect of hydrogen on the mechanical properties of high purity iron I. Softening and hardening of high purity iron by hydrogen charging during tensile deformation. *Mater. Sci. Eng.* **40**, 207–216 (1979).
8. Martin, M. L., Dadfarnia, M., Nagao, A., Wang, S. & Sofronis, P. Enumeration of the hydrogen-enhanced localized plasticity mechanism for hydrogen embrittlement in structural materials. *Acta Mater.* **165**, 734–750 (2019).
9. Gong, P., Nutter, J., Rivera-Diaz-Del-Castillo, P. E. J. & Rainforth, W. M. Hydrogen embrittlement through the formation of low-energy dislocation nanostructures in nanoprecipitation-strengthened steels. *Sci. Adv.* **6**, eabb6152 (2020).
10. Birenis, D. et al. Interpretation of hydrogen-assisted fatigue crack propagation in bcc iron based on dislocation structure evolution around the crack wake. *Acta Mater.* **156**, 245–253 (2018).
11. Song, J. & Curtin, W. A. Atomic mechanism and prediction of hydrogen embrittlement in iron. *Nat. Mater.* **12**, 145–151 (2013).
12. Wang, S., Hashimoto, N. & Ohnuki, S. Hydrogen-induced change in core structures of {110}[111] edge and {110}[111] screw dislocations in iron. *Sci. Rep.* **3**, 2760 (2013).
13. Koyama, M. et al. Origin of micrometer-scale dislocation motion during hydrogen desorption. *Sci. Adv.* **6**, eaaz1187 (2020).
14. Yin, S. et al. Hydrogen embrittlement in metallic nanowires. *Nat. Commun.* **10**, 2004 (2019).
15. Katzarov, I. H., Pashov, D. L. & Paxton, A. T. Hydrogen embrittlement I. Analysis of hydrogen-enhanced localized plasticity: effect of hydrogen on the velocity of screw dislocations in α-Fe. *Phys. Rev. Mater.* **1**, 033602 (2017).
16. Kirchheim, R. Solid solution softening and hardening by mobile solute atoms with special focus on hydrogen. *Scr. Mater.* **67**, 767–770 (2012).
17. Yu, P., Cui, Y., Zhu, G., Shen, Y. & Wen, M. The key role played by dislocation core radius and energy in hydrogen interaction with dislocations. *Acta Mater.* **185**, 518–527 (2020).
18. Cottrell, A. H. & Bilby, B. A. Dislocation theory of yielding and strain ageing of iron. *Proc. Phys. Soc. Sect. A* **62**, 49–62 (1949).
19. Schoeck, G. & Seeger, A. The flow stress of iron and its dependence on impurities. *Acta Metall.* **7**, 469–477 (1959).
20. Shih, D. S., Robertson, I. M. & Birnbaum, H. K. Hydrogen embrittlement of α titanium: in situ TEM studies. *Acta Metall.* **36**, 111–124 (1988).
21. Bond, G. M., Robertson, I. M. & Birnbaum, H. K. Effects of hydrogen on deformation and fracture processes in high-purity aluminium. *Acta Metall.* **36**, 2193–2197 (1988).
22. Matsumoto, T., Eastman, J. & Birnbaum, H. K. Direct observations of enhanced dislocation mobility due to hydrogen. *Scr. Metall. Mater.* **15**, 1033–1037 (1981).
23. Rozenak, P., Robertson, I. M. & Birnbaum, H. K. HVEM studies of the effects of hydrogen on the deformation and fracture of AISI type 316 austenitic stainless steel. *Acta Metall. Mater.* **38**, 2031–2040 (1990).
24. Tabata, T. & Birnbaum, H. K. Direct observations of the effect of hydrogen on the behavior of dislocations in iron. *Scr. Metall. Mater.* **17**, 947–950 (1983).
25. Xie, D. et al. Hydrogenated vacancies lock dislocations in aluminium. *Nat. Commun.* **7**, 13341 (2016).
26. Song, J. & Curtin, W. A. Mechanisms of hydrogen-enhanced localized plasticity: an atomistic study using α-Fe as a model system. *Acta Mater.* **68**, 61–69 (2014).
27. Vitek, V. Core structure of screw dislocations in body-centred cubic metals: relation to symmetry and interatomic bonding. *Philos. Mag.* **84**, 415–428 (2004).
28. Maresca, F., Dragoni, D., Csányi, G., Marzari, N. & Curtin, W. A. Screw dislocation structure and mobility in body centered cubic Fe predicted by a Gaussian approximation potential. *npj Comput. Mater.* **4**, 69 (2018).
29. Wen, M., Fukuyama, S. & Yokogawa, K. Atomistic simulations of effect of hydrogen on kink-pair energetics of screw dislocations in bcc iron. *Acta Mater.* **51**, 1767–1773 (2003).
30. Itakura, M., Kaburaki, H., Yamaguchi, M. & Okita, T. The effect of hydrogen atoms on the screw dislocation mobility in bcc iron: a first-principles study. *Acta Mater.* **61**, 6857–6867 (2013).

31. Chen, X. et al. In situ atomic-scale observation of inhomogeneous oxide reduction. *Chem. Commun.* **54**, 7342–7345 (2018).

32. Shan, Z. W. et al. Mechanical annealing and source-limited deformation in submicrometre-diameter Ni crystals. *Nat. Mater.* **7**, 115–119 (2008).

33. Xie, D. et al. In situ study of the initiation of hydrogen bubbles at the aluminium metal/oxide interface. *Nat. Mater.* **14**, 899–903 (2015).

34. Hirth, J. P. Effects of hydrogen on the properties of iron and steel. *Metall. Trans. A* **11**, 861–890 (1980).

35. Hale, L. M. & Becker, C. A. Vacancy dissociation in body-centered cubic screw dislocation cores. *Comput. Mater. Sci.* **135**, 1–8 (2017).

36. Cheng, B., Paxton, A. T. & Ceriotti, M. Hydrogen diffusion and trapping in α-iron: the role of quantum and anharmonic fluctuations. *Phys. Rev. Lett.* **120**, 225901 (2018).

37. Kimizuka, H. & Ogata, S. Slow diffusion of hydrogen at a screw dislocation core in α-iron. *Phys. Rev. B* **84**, 024116 (2011).

38. Ramasubramaniam, A., Itakura, M. & Carter, E. A. Interatomic potentials for hydrogen in α–iron based on density functional theory. *Phys. Rev. B* **79**, 174101 (2009).

39. Zhu, T., Li, J., Samanta, A., Leach, A. & Gall, K. Temperature and strain-rate dependence of surface dislocation nucleation. *Phys. Rev. Lett.* **100**, 025502 (2008).

40. Chen, D., Costello, L. L., Geller, C. B., Zhu, T. & McDowell, D. L. Atomistic modeling of dislocation cross-slip in nickel using free-end nudged elastic band method. *Acta Mater.* **168**, 436–447 (2019).

41. Gordon, P., Neeraj, T., Li, Y. & Li, J. Screw dislocation mobility in bcc metals: the role of the compact core on double-kink nucleation. *Model. Simul. Mater. Sci. Eng.* **18**, 085008 (2010).

42. Narayanan, S., McDowell, D. L. & Zhu, T. Crystal plasticity model for bcc iron atomistically informed by kinetics of correlated kinkpair nucleation on screw dislocation. *J. Mech. Phys. Solids* **65**, 54–68 (2014).

43. Huang, S., Chen, D., Song, J., Zhu, T. & McDowell, D. L. Hydrogen embrittlement of grain boundaries in nickel: an atomistic study. *npj Comput. Mater.* **4**, 69 (2017).

44. Sun, B. et al. Chemical heterogeneity enhances hydrogen resistance in high-strength steels. *Nat. Mater.* **20**, 1629–1634 (2021).

45. Robertson, I. M. The effect of hydrogen on dislocation dynamics. *Eng. Fract. Mech.* **68**, 671–692 (2001).

Methods

Sample preparation

Rectangular lamellae with dimensions of ~30 × 20 × 5 μm³ were cut from a one-side polished single-crystalline α-iron disk (in which the purity of the used iron was ~99.99%) using a focused ion beam (FIB) instrument FEI Helios NanoLab 600, operated at 30 keV. The so-prepared sample was then transferred and mounted to a mechanical testing rig using the built-in FIB lift-out system. The cylindrical pillars with diameters of ~300 nm and an aspect ratio (length/diameter) of ~3 were fabricated on the lift-out lamellae using the same FIB instrument. To minimize any potentially harmful side effects stemming from the Ga⁺-beam-induced irradiation damage and geometrical tapering of the sample longitudinal shape, the milling current in the final step was reduced to values below 20 pA. A platinum layer of ~150 nm thickness (as shown in Fig. 2a) was formed on the top of the pillar to protect it from non-uniform contact with the diamond punch during cyclic compression tests, thereby avoiding contact-induced dislocation emission. This experimental design provided well-controlled and repeatable contact boundary conditions.

In situ mechanical tests

All mechanical in situ tests were carried out inside of a Hitachi H-9500 ETEM using a Hysitron PI95 H1H sample holder. The holder was equipped with a flat diamond punch that was driven by a microelectromechanical systems transducer. The transducer operated at a force resolution of ~300 nN and a displacement resolution of ~2 nm. Both the mechanical loading direction and the electron-beam direction were oriented along the <100> crystallographic axis of the α-iron sample. Monotonic uniaxial compression tests were performed under displacement control mode at a strain rate of ~5×10^{-3} s⁻¹. The cyclic compression and relaxation tests were conducted in load control mode, and the period of each cycle was 2 s (1.0 s loading + 1.0 s unloading). The applied stress that was imposed during each cycle oscillated from a valley stress to a peak stress to carefully and step-wise manipulate the movement of the mobile dislocations. Hydrogenation of the pillar was conducted under an electron-beam intensity of ~1.2 nA μm⁻² in a 2 Pa H₂ environment. Degassing lasted over a period of 3 h under a high vacuum (<5×10^{-4} Pa) under switched-off electron-beam conditions. Real-time videos of the in situ mechanical tests were recorded using a Gatan 832 charge-coupled device camera, operated at an image acquisition rate of 10 frames per second.

Atomistic simulation

Supplementary Fig. 8 shows the simulation cell containing a right-handed ½<111>{110} screw dislocation at its fully relaxed state. Relaxation was conducted by the conjugate gradient method. The simulation cell has dimensions of 5.6 × 5.6 × 47.5 nm³ and contains a total number of ~80,000 atoms. A periodic boundary condition was imposed along the dislocation line (z-[111] direction), while the surfaces along the x-[211] and y-[011] directions were maintained traction-free. A 0.6-nm-thick layer was fixed at the top and bottom surfaces of the simulation cell in the y direction, respectively. The shear load was exerted by imposing a displacement-controlled boundary condition on the top slab, while the bottom slab was held fixed. We performed NEB calculations with an embedded atom method potential of FeH[38] using the atomistic simulation package LAMMPS (version 29 OCT 2020)[46]. Molecular dynamics simulations were also performed to understand the effect of hydrogen on the critical stress for dislocation motion at room temperature with the same simulation set-up. A constant shear strain rate of 1×10^{8} s⁻¹ was exerted in the canonical ensemble. The hydrogen atoms were randomly introduced into the region around the dislocation core. The hydrogen concentration at the dislocation line is around 0.4 nm⁻¹. To obtain the average virial stress, we performed 20 independent sets of molecular dynamics simulations using the canonical ensemble with random initial velocities. The visualization tool OVITO (version 3.3.0)[47] was used to perform common neighbour analysis to clearly show the screw dislocation.

Data availability

The data that support the findings of this study are available from the corresponding authors upon reasonable request.

References

46. Plimpton, S. Fast parallel algorithms for short-range molecular dynamics. *J. Comput. Phys.* **117**, 1–19 (1995).
47. Stukowski, A. Visualization and analysis of atomistic simulation data with OVITO—the Open Visualization Tool. *Model. Simul. Mater. Sci. Eng.* **18**, 015012 (2009).

Author contributions

Z.S. and D.X. designed and supervised the project. L.H. and D.X. conducted the experiments and analysed the experimental data. D.C. performed the simulations under the guidance of T.Z. and Y.Z.; L.H., D.X. and D.C. wrote the paper with input from S.L., Z.S., E.M., J.L., T.Z. and D.R. All authors contributed to discussions of the results and the revision of the manuscript.

Competing interests

The authors declare no competing interests.

Additional information

Supplementary information The online version contains supplementary material available at https://doi.org/10.1038/s41563-023-01537-w.

Correspondence and requests for materials should be addressed to Degang Xie or Zhiwei Shan.

Peer review information *Nature Materials* thanks the anonymous reviewers for their contribution to the peer review of this work.

Reprints and permissions information is available at www.nature.com/reprints.

Quantitative tests revealing hydrogen-enhanced dislocation motion in α-iron

In the format provided by the authors and unedited

Supplementary Information

This part includes:

        Legends for Supplementary Movies 1 to 6

        Supplementary Figures 1 to 8

        Supplementary Table 1

        Supplementary Notes 1 to 6

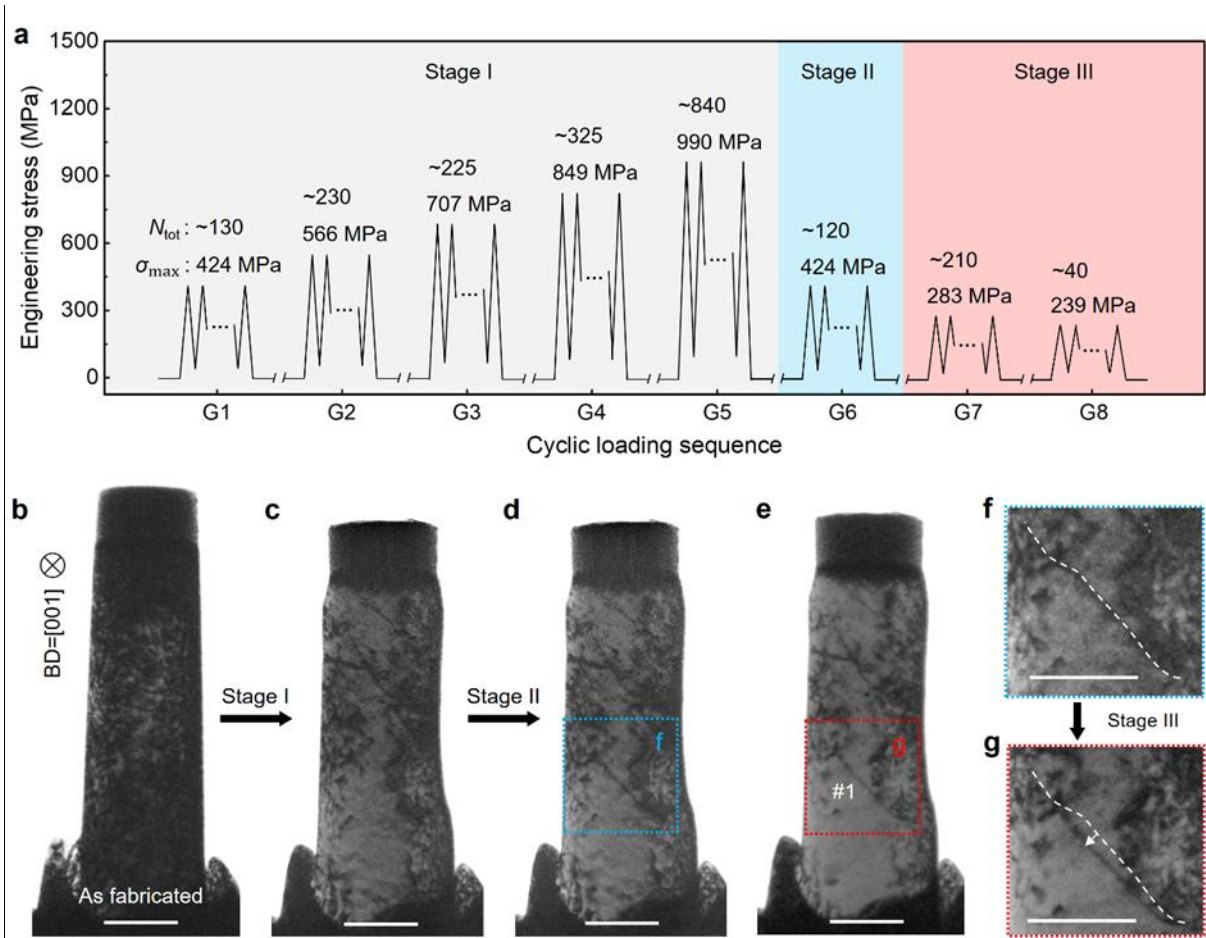   Supplementary References (1 to 12)

Other Supplementary Materials for this manuscript include the following:

        Supplementary Movies 1 to 6

Supplementary Figures:

Supplementary Fig. 1 | Detailed experimental procedure for the small-strain-amplitude cyclic compression of the α-iron pillar. (**a**) Schematic of the cyclic loading sequences applied on the pillar, in which the σ_{max} and total number of cycles (N_{tot}) in each sequence are given. (**b**) The as-fabricated α-iron pillar containing high dislocation density. (**c**) The pillar image after the stage I mechanical annealing, showing dramatically decreased dislocation density. (**d**) and (**e**) The pillar images after stage II and III mechanical annealing, respectively. The dislocation #1 showing reversible bow-out motion between pinning points was obtained. (**f**) and (**g**) are the magnified images of the boxed region in (d) and (e), respectively. The profile of dislocation #1 at σ_{min} in (f) is delineated with white dashed line; the dislocation #1 was further stabilized via a straightening process (stage III cyclic loading), as marked with white arrow in (g). All scale bars are 200 nm.
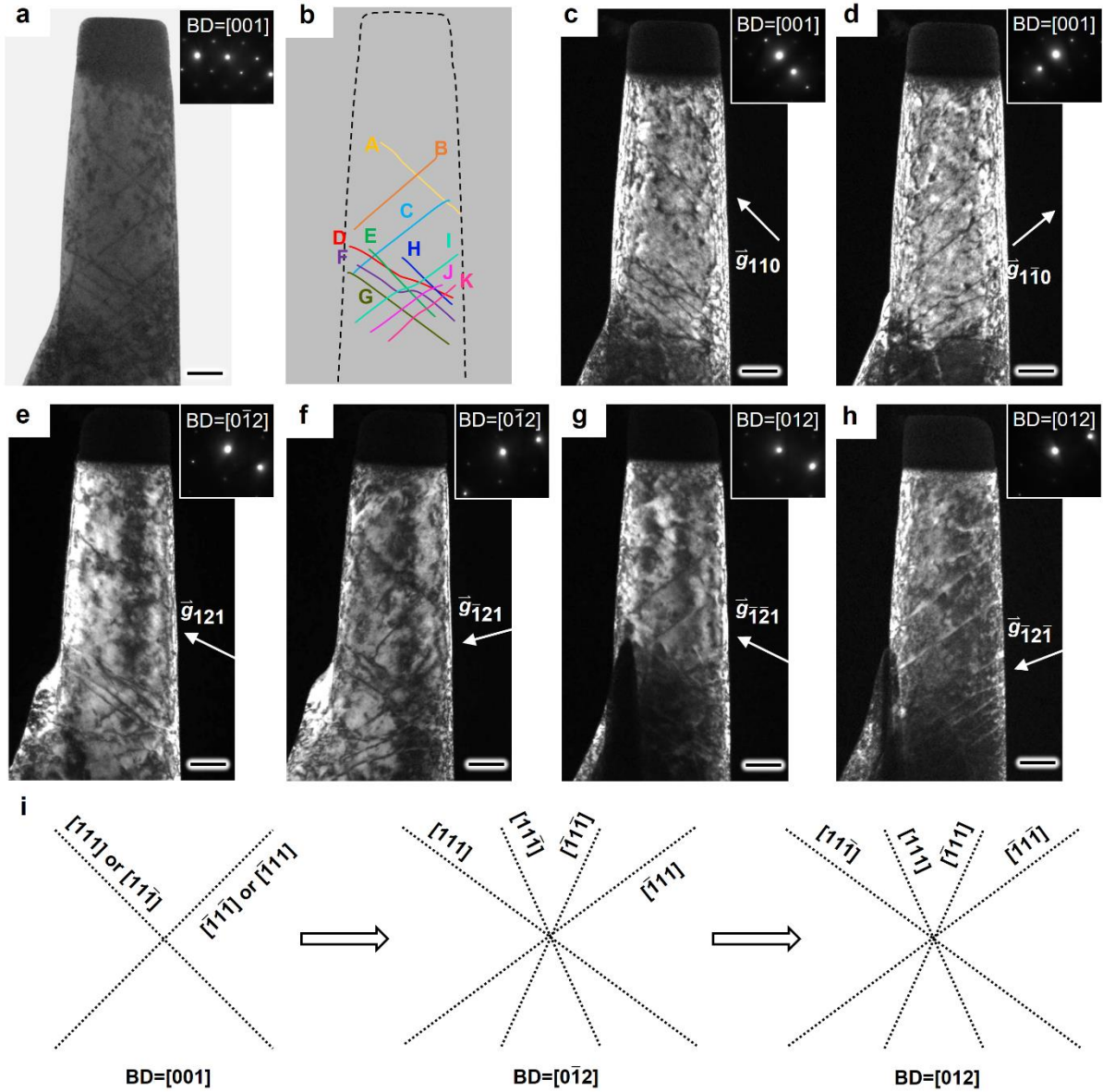
Supplementary Fig. 2 | Determination of the Burgers vectors and the dislocation type (screw or edge) of individual long straight dislocations inside a mechanically-annealed α-iron pillar via the *g·b* criterion. (**a**) A mechanically-annealed pillar showing a few long straight dislocations inside. (**b**) schematically delineates these dislocations as colored solid lines and numbers them alphabetically. (**c**)-(**h**) Dark-field TEM images recorded using various two-beam conditions and diffraction vectors (***g***-vectors). (**i**) shows all possible projected profiles of pure screw dislocation lines with ½<111> Burgers vectors under beam directions (BDs) of [001], [$0\bar{1}2$] and [012]. The contrast of the dislocations in the pillar based on *g·b* criterion are shown in Supplementary Table 1, indicating all the considered dislocations have ½<111> Burgers vectors. Comparing the line directions of these dislocations and their Burgers vectors with the dotted lines shown in (i), the characters of these dislocations can be well identified as screw type. All scale bars are 100 nm.

41
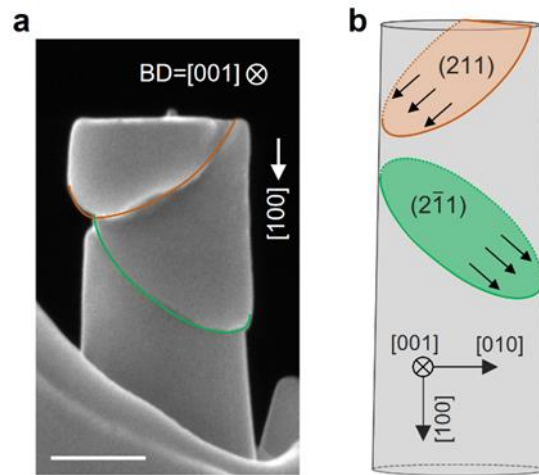
Supplementary Fig. 3 | Slip planes of α-iron under [100]-oriented monotonic compression. (**a**) Postmortem SEM image of a typical pillar (diameter ~290 nm) after monotonic compression which were performed under displacement control by a rate of 0.005 s^{-1}. (**b**) The shear bands show {112}-plane slips, and the orange and green lines represent traces of (211) and ($2\bar{1}1$) slip planes, respectively. The Schmid factor is calculated to be 0.471. The scale bar is 200 nm.

46

47

48
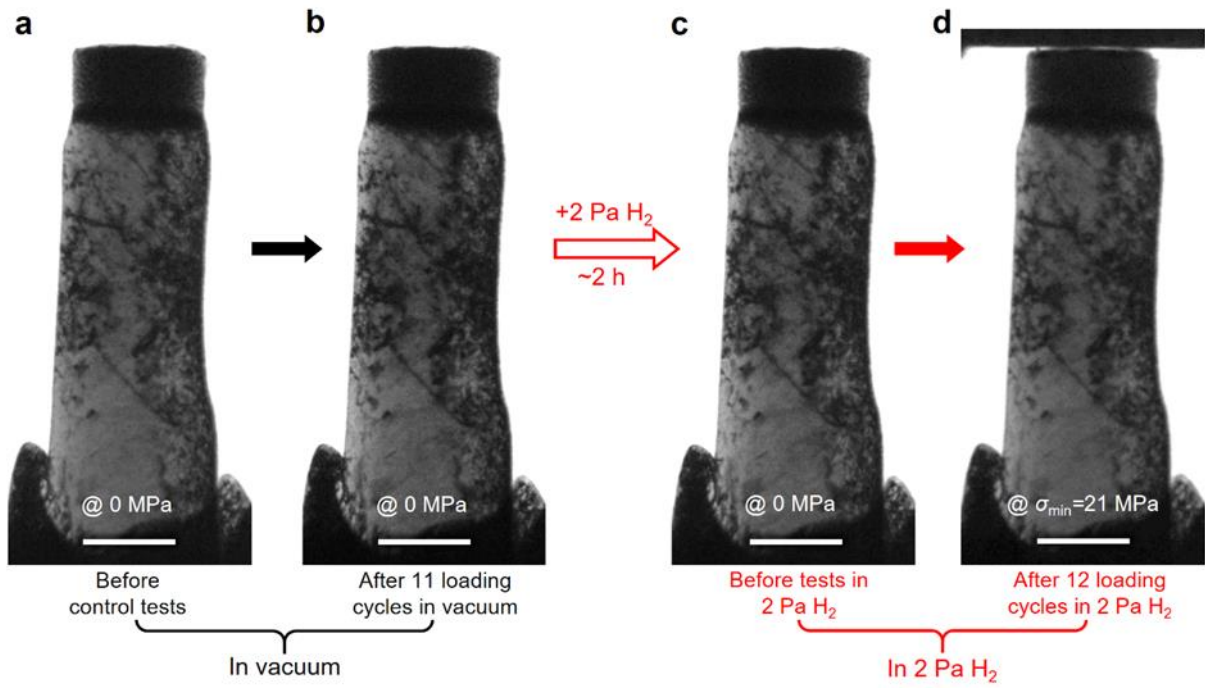
Supplementary Fig. 4 | The microstructures of the pillar at different moments in time, showing almost no visible change throughout the hydrogenation process and the control experiments. (**a**) and (**b**) TEM images of the pillar before control tests (in vacuum) and after 11 loading cycles in vacuum, respectively. (**c**) and (**d**) TEM images of the pillar before and after 12 loading cycles in 2 Pa H_2, respectively. All scale bars are 200 nm.
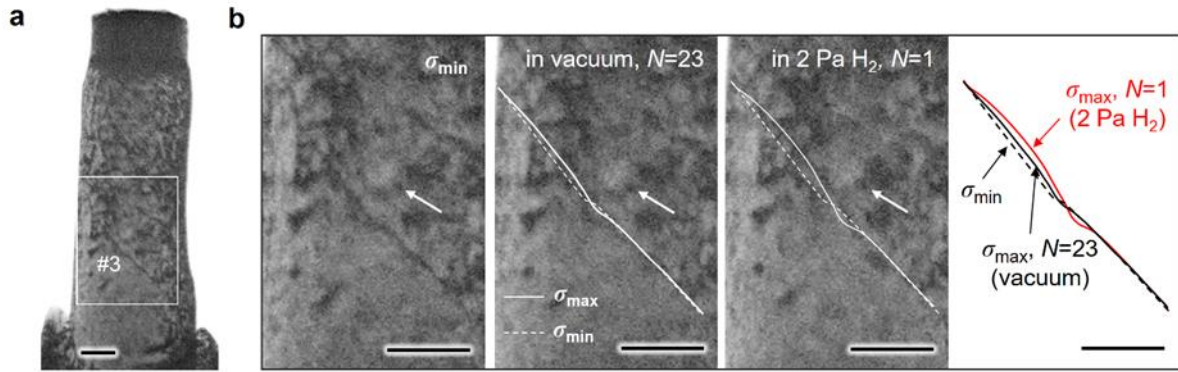
Supplementary Fig. 5 | Effect of hydrogenation on the behaviors of dislocation #3. (**a**) A mobile dislocation numbered #3 inside the α-iron pillar. (**b**) The configurations of dislocation #3 at different states, i.e. at σ_{min} (~21 MPa), at σ_{max} (~211 MPa) in vacuum and at σ_{max} in 2 Pa H_2. The dashed lines and the solid lines indicate dislocation #3's shape and position at σ_{min} and at σ_{max}, respectively. Shown in the rightmost in (b) is the superposed configurations of dislocation #3 at σ_{min} and σ_{max} in both vacuum ($N = 23$) and 2 Pa H_2 ($N = 1$). (**c**) and (**d**) The measured δ_{max} and σ_c of dislocation #3 as a function of loading cycle number in vacuum, and in 2 Pa H_2, respectively. Errors for measurements of δ_{max} and σ_c are ±1.4 nm and ±9.5 MPa, respectively. Error bars represent standard deviation. The tests in 2 Pa H_2 were started after that the sample had been exposed to the 2 Pa H_2 atmosphere for ~2 hours. All scale bars, 100 nm.
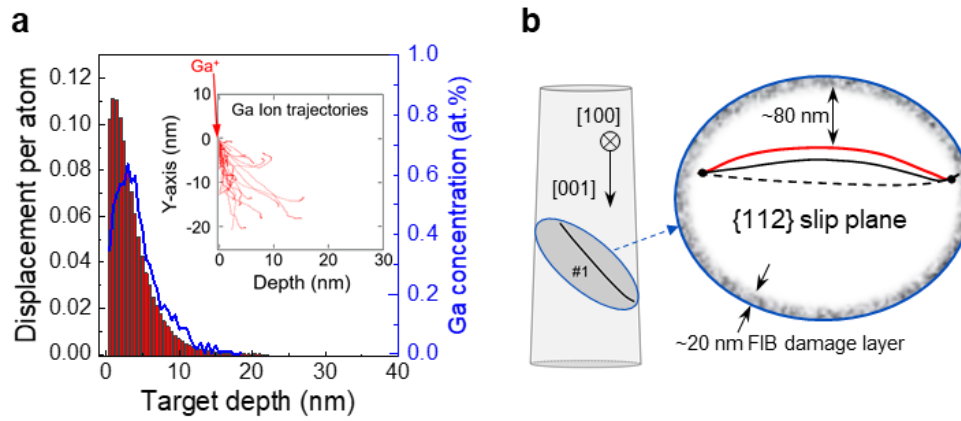
Supplementary Fig. 6 | Illustration of the distribution of FIB-induced surface defects and the motion of dislocation #1. (a) SRIM-based Monte Carlo calculations showing the displacements per atom for Fe and the projected distribution of implanted Ga$^+$ ions as a function of target depth. The inset shows the SRIM predictions for the trajectories of 200 implanted Ga ions. **(b)** Schematic of the dislocation #1 in the slip plane viewed from the normal direction.
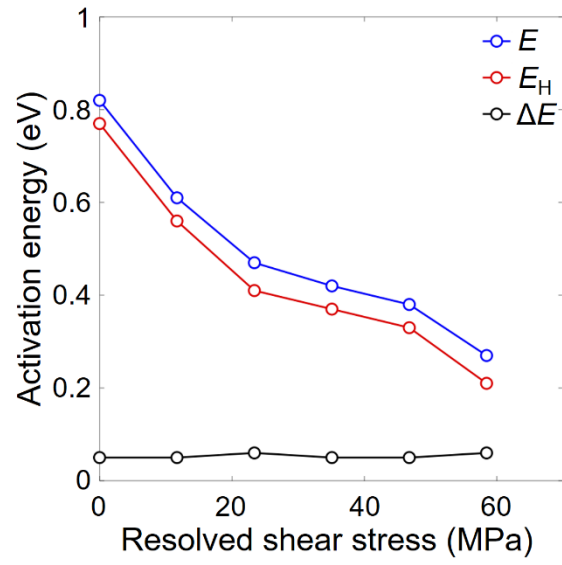
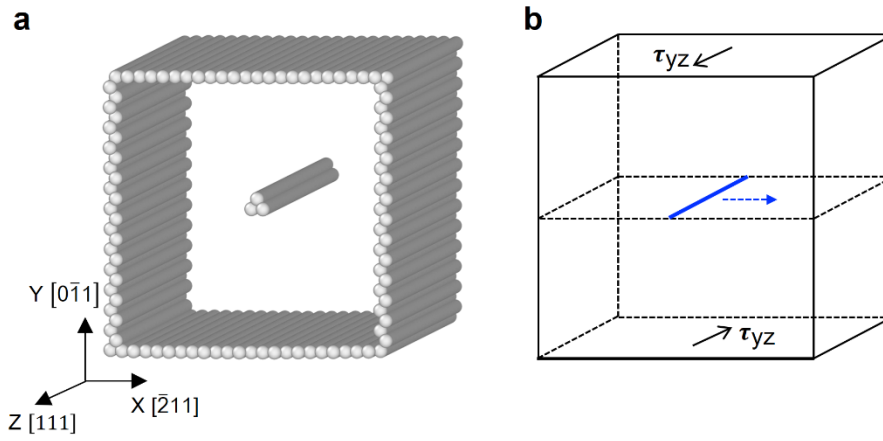**Supplementary Fig. 7 | Stress-dependent activation energies.** The stress-dependent activation energies reveal that the reduction of energy barrier ($\Delta E = E - E_H = 0.05$ eV) is not sensitive to the resolved shear stress.

Supplementary Fig. 8 | Atomistic simulation setup. (a) 3D perspective view of the supercell and the right-hand screw dislocation. Atoms with perfect BCC structure inside the structure are removed to display the surfaces and core structure of screw dislocation. (**b**) Schematic of the supercell showing details of the applied shear stress τ_{yz} and the direction of dislocation glide. The blue line indicates the screw dislocation.

Supplementary Table:

Supplementary Table 1 | Characterization of the Burgers vector of dislocations delineated in Supplementary Fig. 2b using the **g·b** criterion.

Dislocation	g-vector						b-vector
	[110]	[1$\bar{1}$0]	[121]	[$\bar{1}$2$\bar{1}$]	[$\bar{1}$2$\bar{1}$]	[12$\bar{1}$]	
A	√	×	√	√	×	√	±½[111]
B	×	√	×	√	√	√	±½[1$\bar{1}$1]
C	×	√	×	√	√	√	±½[1$\bar{1}$1]
D	√	×	√	√	×	√	±½[111]
E	√	×	√	√	×	√	±½[111]
F	√	×	√	√	×	√	±½[111]
G	√	×	√	×	√	√	±½[11$\bar{1}$]
H	√	×	√	√	×	√	±½[111]
I	×	√	×	√	√	√	±½[1$\bar{1}$1]
J	×	√	×	√	√	√	±½[1$\bar{1}$1]
K	×	√	×	√	√	√	±½[1$\bar{1}$1]

* '√' means visible, while '×' means invisible in TEM images shown in Supplementary Fig. 2

Supplementary Notes:

Supplementary Note 1. <u>Mechanical annealing treatment of FIBed α-iron pillar.</u>

The as-fabricated single-crystal iron pillar contained a high density of pre-existing dislocations, making it difficult to track the behavior of individual dislocations without the influence of neighboring dislocations. To reduce the dislocation density inside the pillar and thus facilitate the observation of individually isolated dislocations, we applied the mechanical annealing treatment through a series of moderate cyclic compression and relaxation for promoting dislocation escape and annihilation (Supplementary Fig. 1). Since the Peierls stress of screw dislocations is at least one order of magnitude larger than that of edge dislocations in BCC crystals at room temperature due to their non-planar core structure[1], the mobility of screw components of a generally curved dislocation is intrinsically much lower than that of edge components. It follows that the applied stress can drive the edge components out of the pillar quickly. After the mechanical annealing treatment, most mixed dislocations have been transformed to screw ones with a Burgers vector ½<111>, as shown by the characterization results in Supplementary Fig. 2 and Supplementary Table 1. Such screw dislocations usually form long straight lines along the <111> Peierls valleys, pinned by defects near the free surface, such as dislocation loops, point-defect clusters or sessile dislocation debris, as shown in Fig. 1b.

As suggested in the literature[2–4], such motion of a curved dislocation between pinning points involves the rate-limiting process of kink-pair nucleation at its leading screw segment when the bow-out distance is relatively small. Hence, we constrained the peak stress in the ensuing mechanical cycles to produce a small dislocation bow-out at the low peak stress. The resulting stable and reversible bow-out configurations neither added nor removed pinning points, ensuring kink-pair nucleation as the rate-controlling mechanism during the whole process. In this way, we were able to reproduce the nearly identical bow-out motion of the same dislocation segment hundreds of times, thereby enabling the quantitative and repeatable comparison of the kinetic parameters of dislocation motion under different loading atmospheres (see Fig. 1d).

Supplementary Note 2. <u>Motion of dislocation #3 before and after hydrogenation</u>.

The dislocation #3 was also characterized as screw-dominant type with a 'z'-shaped kink at the middle, as shown in Supplementary Fig. 5a-b. Before the control experiments on dislocation #3, the sample was subjected to a three-day aging in vacuum drying autoclave ($\sim 1\times 10^4$ Pa). Then, the dislocation #3 was firstly tested in vacuum for a total of 23 consecutive cycles with the same loading parameters as that used on dislocation #1. Under cyclic loading the dislocation #3 also exhibited a steady forward-and-back type motion, where the 'z'-shaped kink was also mobile, as shown in Supplementary Fig. 5b and Supplementary Movie 3. Later the pillar was exposure to ~ 2 Pa H_2 for ~ 2 h

107   under electron beam illumination. After hydrogenation, the configuration of dislocation #3 remained unchanged and

108   then the same loading function was applied for 20 cycles (see Supplementary Movie 4).

109   As shown in Supplementary Fig. 5b-d, it's clearly seen that the bow-out movement of dislocation #3 exhibited a

110   larger amplitude after hydrogenation (average δ_{max} = 12.3±2.3 nm) than before hydrogenation (average δ_{max} = 7.5±0.6

111   nm). In addition, as shown in Supplementary Fig. 5c and 5d, the measured σ_c was reduced by ~27% from 98.2±8.9

112   MPa to 72.0±11.2 MPa on average after hydrogenation process.

113   **Supplementary Note 3. <u>Hydrogen modification of elastic interaction between dislocation#1 and near-surface</u>**

114   **<u>defects.</u>**

115   In a pure single-crystal α-iron pillar, most defects such as point-defect clusters, sessile dislocation loops and Ga/Pt

116   solute atoms were produced during the FIB milling process. However, these FIB-induced defects mainly reside near

117   the free surface and could be evaluated using SRIM-based Monte Carlo simulations[5]. Supplementary Fig. 6a shows

118   that under our FIB milling condition, the depth of Ga^+ penetration and thus FIB induced defects are less than 22 nm

119   beneath the surface. Based on these results, Supplementary Fig. 6b shows a schematic illustration of the damage layer

120   and dislocation #1 (scaled to their actual sizes) in the pillar's cross section. It is seen that the middle part of the

121   dislocation segment, where the rate-controlling mechanism of kink-pair nucleation operates, is sufficiently away from

122   the near-surface defects by a distance of ~80 nm. Calculations by Birnbaum & Sofronis[6] show that the shielding

123   effect becomes important only at a relatively high bulk hydrogen concentration (e.g. 10^3~10^5 atom ppm.) and a short

124   separation distance between the dislocation and other stress centers (<20b). In our experiments, as shown in

125   Supplementary Fig. 6b, the middle part of the dislocation#1 is always >>20b from those near-surface defects, and

126   thus the hydrogen modification of elastic interaction mainly affect the dislocation parts close to both ends.

127   However, the hydrogen effects on these lattice defects and the elastic interactions between them were suggested as a

128   contributing factor to the observed increased fluctuations in δ_{max} after hydrogenation, as indicated in Fig. 2d and 2e,

129   where the measured standard deviation of δ_{max} was increased from ~0.6 to ~3.3 nm. Such increased fluctuations

130   might arise from the following factors. First, the redistribution of hydrogen can occur in the sample and thus is not

131   exactly identical in all the cycles, due to changes of the position of the dislocation and other trapping sites such as

132   point defects. Hence, the hydrogen-dislocation interactions vary slightly in different cycles. In contrast, if all lattice

133   defects remain unchanged, the hydrogen can maintain its original distribution, as thermal activation is below the

134   trapping depth[7,8]. Second, there may be hydrogen-induced changes of the local stress fields and associated elastic

135   interactions between the surface defects and dislocation parts close to the pinning points, but these changes should

136 play a minor role in the observed hydrogen effect on dislocation behavior.

137 **Supplementary Note 4. <u>Diminishing effect of the hydrogen-enhanced dislocation motion.</u>**

138 One plausible explanation of delayed hydrogen release and the gradual restoration of dislocation behavior is the de-

139 trapping of hydrogen from moving dislocations (rather than from vacancies). On the one hand, hydrogen in α-iron

140 has a lower binding energy at the screw dislocation core ($E_{\text{H-screw}}$ = 0.26~0.29 eV) compared to vacancies ($E_{\text{H-Vac}}$ =

141 0.56~0.64 eV)[8,11], thus making hydrogen detachment from screw dislocations easier. On the other hand, vacancies

142 are almost immobile under the stresses applied, due to their spherical stress field which is insensitive to shear stresses;

143 in contrast, screw dislocations readily move upon shear loading by nucleation, propagation and annihilation of kink-

144 pairs, thus helping to shake off the attached hydrogen. The fact that the hydrogen-induced enhancement in dislocation

145 motion gradually faded with successive oscillating motion of dislocations also indicates that for each load cycle, only

146 a small part of the attached hydrogen atoms was shaken off, and thus multiple load cycles were required to exhaust

147 the weakly trapped hydrogen from the screw dislocation lines. Also, the motion of screw dislocations requires kink-

148 pairs, which have edge character. This means that some hydrogen atoms detrapped from dislocations/vacancies can

149 become re-trapped at these kinks, before finally being shaken off with repeated cycling. Such mechanically-assisted

150 degassing effect suggests that to further eliminate dissolved hydrogen in metals, mechanical treatment can be an

151 effective means, in addition to traditional thermal annealing treatments. Hence, mitigation or even elimination of the

152 hydrogen-enhanced local plasticity effect is only possible when hydrogen trapped at dislocations is 'shaken off' by

153 cyclic mechanical loading.

154 **Supplementary Note 5. <u>Asymmetry of the minimum energy path in NEB calculation.</u>**

155 Theoretically, the minimum energy path (MEP) should be symmetry at zero stress. As the shear stress increases, the

156 MEP is tilted, and the intermediate saddle-point energy is reduced accordingly. As a result, under the resolved shear

157 stress τ_{yz} = 24 MPa, the MEP shown in Fig. 4a is tilted. In addition, due to the free boundary conditions in the

158 dislocation motion direction (X direction in Supplementary Fig. 8), the image forces from two surfaces may not be

159 the same, intensifying the extent of the asymmetry.

160 **Supplementary Note 6. <u>Electron densities and embedding energies of H in the interstitial sites.</u>**

161 The H-induced decrease of kink-pair nucleation barrier could be attributed to the electron density effect[12]. The effect

162 of electron density is represented by the EAM potential[11] as follows

163
$$E_j = F_\beta\left(\sum_{i\neq 1} \rho_{\alpha\beta}(r_{ij})\right) + \frac{1}{2}\sum_{i\neq j} \phi_{\alpha\beta}(r_{ij}) \tag{5}$$

Here E_j is the potential energy of an atom j; r_{ij} is the distance between atom i and j; $\phi_{\alpha\beta}$ is a pairwise potential function; $\rho_{\alpha\beta}$ refers to the normalized electron density contributed by a neighbor atom i of type α at the site of atom j of type β; F_β is the embedding function that represents the energy required to place atom j of type β into the electron cloud. The interaction energy between Fe and H is mainly governed by the embedding energy F_H, depending on the total electron density ρ_H arising from the six nearest iron atoms surrounding a hydrogen atom, i.e.

$$F_H = F_H(\rho_H) = F_H\left(\sum_{i=1}^{6} \rho_{FeH}\left(r_{Fe_iH}\right)\right) \tag{6}$$

Here the ρ_{FeH} is the electron density function from the Fe atom to the H atom, r_{Fe_iH} is the distance between the i-th Fe atom and the H atom.

Supplementary References

1. Bacon, D. J., Osetsky, Y. N. & Rodney, D. Dislocation–obstacle interactions at the atomic level. In: Dislocations in Solids, Vol. 15 (eds Hirth J. P., Kubin L.), 1-90 (Elsevier, 2009).

2. Caillard D. Kinetics of dislocations in pure Fe. Part I. In situ straining experiments at room temperature. Acta Materialia 58, 3493-3503 (2010).

3. Louchet F, Kubin L. P. & Vesely D. In situ deformation of b.c.c. crystals at low temperatures in a high-voltage electron microscope Dislocation mechanisms and strain-rate equation. Philosophical Magazine A 39, 433-454 (1979).

4. Furubayashi E-i. Behavior of Dislocations in Fe-3% Si under Stress. Journal of the Physical Society of Japan 27, 130-146 (1969).

5. Kiener, D., Motz, C., Rester, M., Jenko, M. & Dehm, G. FIB damage of Cu and possible consequences for miniaturized mechanical tests. *Mater. Sci. Eng. A*. **459**, 262-272 (2007).

6. Birnbaum, H. K. & Sofronis, P. Hydrogen-enhanced localized plasticity—a mechanism for hydrogen-related fracture. *Mater. Sci. Eng. A* **176**, 191-202 (1994).

7. Tateyama, Y. & Ohno, T. Stability and clusterization of hydrogen-vacancy complexes in α−Fe:An ab initio study. *Phys. Rev. B* **67**, 174105 (2003).

8. Kimizuka, H. & Ogata, S. Slow diffusion of hydrogen at a screw dislocation core in α-iron. *Phys. Rev. B* **84**, 024116 (2011).

9. Hull, D., Bacon D. J. Introduction to Dislocations. *Butterworth-Heinemann, Oxford*, (2001).

10. Argon, A.S. Strengtheining mechanisms in crystal plasticity. *Oxford University Press,* (2008).

11. Ramasubramaniam, A., Itakura, M. & Carter, E. A. Interatomic potentials for hydrogen in α–iron based on density functional theory. *Phys. Rev. B* **79**, 174101 (2009).

12. Huang, S., Chen, D., Song, J., Zhu, T. & McDowell, D. L. Hydrogen embrittlement of grain boundaries in nickel: an atomistic study. *NPJ Comput. Mater.* **4**, 69 (2017).